

Journal of Materials Chemistry A

Accepted Manuscript



This is an *Accepted Manuscript*, which has been through the Royal Society of Chemistry peer review process and has been accepted for publication.

Accepted Manuscripts are published online shortly after acceptance, before technical editing, formatting and proof reading. Using this free service, authors can make their results available to the community, in citable form, before we publish the edited article. We will replace this *Accepted Manuscript* with the edited and formatted *Advance Article* as soon as it is available.

You can find more information about *Accepted Manuscripts* in the [Information for Authors](#).

Please note that technical editing may introduce minor changes to the text and/or graphics, which may alter content. The journal's standard [Terms & Conditions](#) and the [Ethical guidelines](#) still apply. In no event shall the Royal Society of Chemistry be held responsible for any errors or omissions in this *Accepted Manuscript* or any consequences arising from the use of any information it contains.



ARTICLE

In-situ Incorporation of FeS Nanoparticles/Carbon Nanosheets Composite with An Interconnected Porous Structure as A High-Performance Anode for Lithium Ion Batteries

Received 00th January 20xx,
Accepted 00th January 20xx

DOI: 10.1039/x0xx00000x

www.rsc.org/

Yuanxian Xu,^{ab} Wenyue Li,^{*a} Fan Zhang,^a Xiaolong Zhang,^a Wenjun Zhang,^c Chun-Sing Lee,^c Yongbing Tang^{*a}

Interconnected porous FeS/C composite consisting of FeS nanoparticles (~20 nm) homogeneously embedded in carbon nanosheets was synthesized via a facile freeze-drying/carbonization method using NaCl template. As anode for LIBs, this composite shows significantly enhanced electrochemical performances due to the synergistic effects of the conductive carbon film and the porous structure, which provide an ideal conductive matrix and buffer spaces for respectively electron/ion transfer and FeS expansion during lithiation process. This composite exhibits reversible capacities of ~703 mA h g⁻¹ over 150 cycles at the 1 A g⁻¹ and a high-rate capability of ~530 mA h g⁻¹ even at 5 A g⁻¹, which is among the best reported electrochemical performances for FeS-based materials thus far, demonstrating its potential application in LIBs with long cycling life and high power density.

Introduction

Exploring alternative anode materials for lithium ion batteries (LIBs) has been intensively conducted and constantly promoted in order to satisfy the energy storage and conversion applications demanding for high energy and power densities.¹⁻⁵ Metal sulfides, one class of most promising anode materials for LIBs, show much higher theoretical specific capacities than traditional graphite materials (372 mA h g⁻¹) attracting considerable research.⁶⁻¹⁰ However, they usually have limited conductivity for impacting the electron or ion transport during electrode reactions, thus leading to significant capacity loss.¹¹⁻¹² Pulverization of metal sulfides and subsequent detachment from the current collectors induced by large volume changes during lithium insertion and extraction processes also hinder their commercial application.¹³⁻¹⁵ Furthermore, just like lithium sulfur batteries, a polysulfide shuttling effect may cause the electrochemical degradation of the active metal sulfide materials, resulting in continuous capacity fading upon cycling.¹⁶⁻¹⁸ To address these problems described above, recent researches have primarily focused on two aspects: 1) Structure engineering for introducing abundant free space to alleviate the volume

change effect and activating the electrode surface to facilitate the permeation of lithium ions from the electrolyte to solid electrode (more ion pathways can be provided after surface engineering).¹¹⁻²⁶ For instance, metal sulfides with porous, hollow and core-shell structures have been successfully fabricated and exhibit enhanced electrochemical performances compared with corresponding bulk materials.¹⁹⁻²¹ 2) Composition controlling for increasing their conductivity and stability *via* composing with conductive materials such as graphene, carbon nanotubes and conductive polymer.²²⁻²⁷ These conductive materials not only provide fast electron/ion transport route, but also promote the active materials to form a stable solid electrolyte interface (SEI) film during the first several charge-discharge processes making the structure of metal sulfides stable upon long-term cycling.²²⁻²⁷

Iron sulfide (FeS), as one kind of metal sulfides, completes the lithium ion storage *via* $\text{Li}^+ + \text{FeS} + 2\text{e}^- \rightarrow \text{Li}_2\text{S} + \text{Fe}$ reaction, giving a theoretical specific capacity of 609 mA h g⁻¹.²⁸⁻³⁸ Nevertheless, its electrochemical performances are also seriously restricted by the problems of metal sulfide in common.²⁸⁻³⁰ As suggested above, structure and surface engineering are effective methods to settle these tough obstacles. By employing a combination of electrospinning technique and biomolecular-assisted hydrothermal method, Zhu et al. successfully fabricate porous graphitic carbon nanowires with FeS nanodots accommodating in them.²⁸ Due to the synergetic effect between carbon nanowires and FeS nanodots, this anode shows impressive LIB performances with a discharge capacity of 400 mA h g⁻¹ after 50 cycles at 0.5 C. Xu et al. also reported a carbon coated FeS nanosheets, which are highly active anode materials for LIBs (615 mA h g⁻¹ at a current of 100 mA g⁻¹ after 100 cycles).³⁰ While the reported

^aFunctional Thin Films Research Center, Shenzhen Institutes of Advanced Technology, Chinese Academy of Sciences, Shenzhen, 518055, China. E-mail: tangyb@siat.ac.cn; wy.li@siat.ac.cn

^bNano Science and Technology Institute, University of Science and Technology of China, Suzhou 215123, China

^cDepartment of Physics and Materials Science, Center of Super-Diamond and Advanced Films (COSDAF), The City University of Hong Kong, Hong Kong SAR, China

†Electronic Supplementary Information (ESI) available. See DOI: 10.1039/x0xx00000x

studies suggested that the poor stability of FeS can be optimized by the incorporating carbon, the rational design of FeS based materials with long-term stability and rate capability at high current densities (e.g., higher than 1 A g^{-1}) still remain a challenge.

In this study, an interconnected porous FeS/C composite consisting of carbon nanosheets anchored with well-dispersed FeS nanoparticles (designated as FeS@CNS) were successfully in-situ synthesized via a facile freeze-drying/carbonization approach using sodium chloride (NaCl) crystals as template. The simultaneous formation of carbon nanosheets and FeS nanoparticles on the surface of NaCl templates makes a good incorporation between FeS and carbon nanosheets. Furthermore, the interconnected porous carbon nanosheets as elastic substrate can buffer the volume change of FeS during lithiation/delithiation processes. As a result, when evaluated as anode materials for LIBs, it shows significantly improved electrochemical performances of a capacity $\sim 703 \text{ mA h g}^{-1}$ over 150 cycles at 1 A g^{-1} and $\sim 532 \text{ mA h g}^{-1}$ even at 5 A g^{-1} .

Experimental

Synthetic procedures

The reagents were obtained from Sinopharm Chemical Reagent Co., Ltd. and used as received without any further purification. In a typical synthesis process, 1.35 g ferric chloride hexahydrate ($\text{FeCl}_3 \cdot 6\text{H}_2\text{O}$, 99%), 1.47 g citric acid ($\text{C}_6\text{H}_8\text{O}_7$, 99.5%), 20 g NaCl (99.5%) and 0.76 g thiourea ($\text{CH}_4\text{N}_2\text{S}$, 99%) were dissolved in 100 ml of deionized (DI) water. The solution was frozen under liquid nitrogen surrounding and dried using a lyophilizer. And then, the dry gel was ground into fine powders, loaded into a alumina crucible and heated at $800 \text{ }^\circ\text{C}$ for various times (15 min, 30 min, 1 h and 2 h) in a tube furnace under Ar atmosphere. After cooled to room temperature, the black powder was dispersed into DI water to dissolve the NaCl template. Finally, the FeS@CNS sample was obtained after being filtrated, washed with DI water and alcohol for several times and dried at $60 \text{ }^\circ\text{C}$ in vacuum. For comparison, FeS/C composite was also synthesized using the same procedure described above except adding the NaCl template. FeS particles and porous carbon nanosheets were obtained by calcination of the mixtures of $\text{FeCl}_3 \cdot 6\text{H}_2\text{O}$, $\text{CH}_4\text{N}_2\text{S}$, NaCl and $\text{C}_6\text{H}_8\text{O}_7$ at $800 \text{ }^\circ\text{C}$ after freeze-drying process, respectively.

Materials characterizations

Scanning electron microscopy (SEM) was carried out using a Nova NanoSEM 450 field emission scanning electron microscope with an acceleration voltage of 10 kV. TEM and HRTEM were performed using a TECNAI G² F20 S-Twin electron microscope operated at 200 kV. Powder X-ray diffraction (XRD) analysis was measured on a Rigaku D/Max-2500 diffractometer with Cu K α radiation. Thermogravimetric (TG) measurement (Netzsch-STA 449C) was conducted from room temperature to $900 \text{ }^\circ\text{C}$ at a heating rate of $10 \text{ }^\circ\text{C}/\text{min}$ in air. Raman spectrum was recorded on a LabRAM HR Raman spectrometer using laser excitation at 514.5 nm. Brunauer-

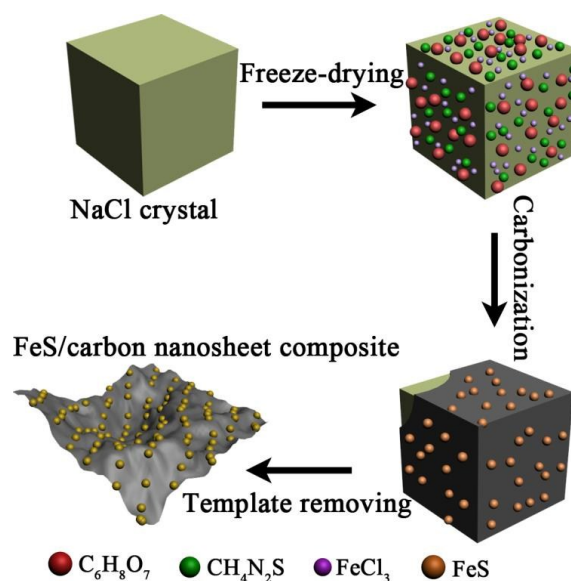
Emmett-Teller (BET) surface areas of the products were determined by nitrogen adsorption and desorption using a Micromeritics ASAP 2020 analyzer at 77 K. X-Ray photoelectron spectroscopy (XPS) spectra were tested on a ESCALAB 250Xi system.

Electrochemical measurements

The electrochemical properties of FeS@CNS, FeS/C, FeS and carbon nanosheets were tested using coin-type half cells (CR2032) assembled at room temperature in an argon-filled glovebox with lithium metal foil as the counter electrode. The anode was fabricated by mixing the active material, carbon black and poly-(vinylidene fluoride) (PVDF) with mass ratio of 80:10:10 in N-methyl-2-pyrrolidone (NMP) to form a homogeneous slurry. Subsequently, the slurry was coated onto a Cu foil, and dried at $80 \text{ }^\circ\text{C}$ for 24 h in a vacuum oven. The modified Cu foil was then pressed and punched into 10 mm diameter electrodes with mass loading of $\sim 1.0 \text{ mg}$. Celgard 2400 and 1 M LiPF_6 in ethylene carbonate/dimethyl carbonate/ethyl methyl carbonate (EC/DMC/EMC, 1:1:1 v/v/v) were respectively used as the separator and electrolyte. The charge/discharge measurement was performed using a LAND CT2001A battery test system over a voltage window from 0.01 to 3 V at room temperature. Cyclic voltammetry (CV) measurement was conducted on a CHI 600D electrochemical workstation at 0.1 mV/s over the range of 0.01–3.0 V. Electrochemical impedance spectroscopy (EIS) analysis was recorded using an Autolab 302N electrochemical workstation in the frequency range from 100 kHz to 10 mHz.

Results and discussion

Scheme 1 shows the typical preparation process of FeS@CNS. Firstly, certain amounts of NaCl, $\text{C}_6\text{H}_8\text{O}_7$, NH_2CSNH_2 and FeCl_3 were dissolved into DI water to form an even solution. Secondly, the DI water was evaporated via a freeze-drying method leading to the uniform distribution of each component in the mixed powder. In this step, the reaction complex ($\text{FeCl}_3 \cdot \text{NH}_2\text{CSNH}_2 \cdot \text{C}_6\text{H}_8\text{O}_7$) can be easily attached on the surfaces of



Scheme 1 Schematic illustration of the fabrication process of FeS@CNS.

the formed NaCl crystals. Thirdly, the fine mixed powder was calcinated at 800 °C under Ar atmosphere for 2h. During this process, the carbon source was carbonized into carbon nanosheets with the assistance of NaCl crystals, simultaneously, the metal precursor FeCl₃ was converted into iron oxides with NH₂CSNH₂ being decomposed into H₂S. Then the iron oxides react with the H₂S to form the FeS nanoparticles anchoring on the carbon nanosheets. Finally, FeS@CNS composite was obtained by removing the NaCl with DI water for several times. It should be noted that the NaCl templates can be easily recycled via evaporating the DI water.^{26,39} In order to clarify the reaction mechanism, FeS/CNS samples annealed for 15 min, 30 min and 1 h have been also prepared. As exhibited in Fig. S1, the XRD peaks of all the three samples are all indexed to the hexagonal FeS (JCPDS Card no.37-0477), indicating that the metal precursor FeCl₃ directly reacts with the H₂S derived from the decomposition of thiourea to form the FeS nanoparticles during the anneal process.

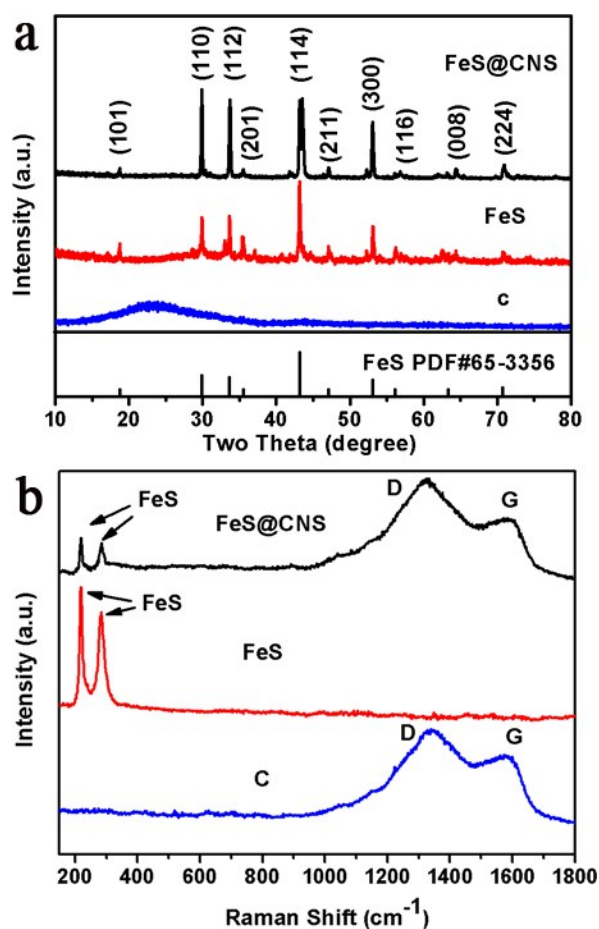


Fig. 2 XRD patterns (a) and Raman spectrum (b) of the FeS@CNS, FeS and carbon samples.

As shown in Fig. 2a, all sharp XRD diffraction peaks of FeS@CNS and FeS can be well indexed to the hexagonal FeS (JCPDS Card no.37-0477), indicating the high degree of crystallinity of the FeS.²⁸⁻²⁹ For carbon sample, only one broad and weak diffraction peak can be observed between 20 and 25

°, which is assigned to the amorphous carbon.⁴⁰ Thermal gravimetric analysis (TGA) curves of FeS@CNS, FeS and carbon are exhibited in Fig. S2. When the sample was heated to 900 °C, the carbon and FeS components were completely oxidized into CO₂ and Fe₂O₃.^{33,36} According to the total 23 % weight loss of FeS@CNS, the weight percentage of carbon is calculated to be ~10.5 %. To better understanding the structure of FeS@CNS composite, Raman spectroscopy of FeS@CNS, FeS and carbon were performed and the results are shown in Fig. 2b. In the sample of carbon, two distinct peaks at ~1350 (D band) and 1600 cm⁻¹ (G band) are presented, which can be assigned to the amorphous and crystalline graphite.^{40,41} For the sample of FeS@CNS, besides two carbon characteristic peaks, two new peaks located at 214 and 282 cm⁻¹ are observed which are typical asymmetric and symmetric stretching modes of FeS.⁴² The XPS analysis was further carried out to evaluate the composite of FeS@CNS. From the Fig. S3, peak located at ~707 eV is assigned to the Fe 2P_{3/2} of the Fe²⁺, which is the characteristic peak of the FeS.^{46,47} And the peaks at ~161.4 and 163.1 eV are indexed to the S 2p_{3/2} and S 2p_{1/2} respectively.^{46,47} The survey of the XPS are also consistent with the results of the Raman and XRD tests.

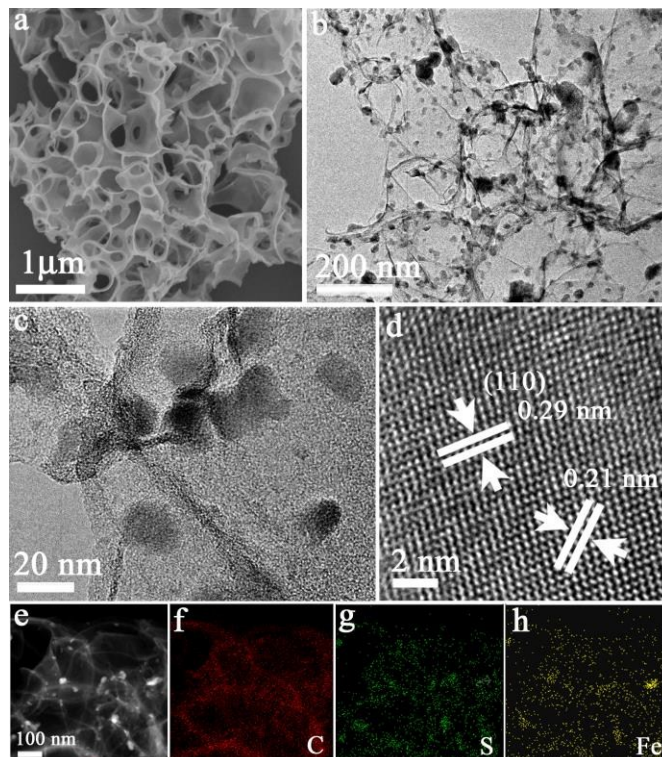


Fig. 3 SEM (a) TEM (b, c) HRTEM (d) and STEM (e) images of the FeS@CNS; EDS mapping of carbon (f), sulfur (g) and iron (h) elements.

Fig. 3a shows a typical SEM image of FeS@CNS. It can be seen that these carbon nanosheets are interconnected together to form porous networks with pore size ranging from hundreds nanometers to micrometer. Consequently, the FeS@CNS composite can be effectively infiltrated by the electrolyte achieving a fast electrode activation process during the battery operation. For comparison, SEM images of FeS/C and FeS samples are also shown in Fig. S4, only large

microparticles can be obtained without adding the NaCl crystal template, confirming the NaCl crystal can provide abundant surfaces for reaction and avoid FeS product from agglomeration during the anneal step. As a result, the specific surface area of FeS@CNS is about $312.0 \text{ m}^2 \text{ g}^{-1}$ (Fig. S5), which is much larger than that of FeS/C ($82.8 \text{ m}^2 \text{ g}^{-1}$) and FeS ($23.0 \text{ m}^2 \text{ g}^{-1}$). The results can also be verified by the density of the three samples. As shown in Fig. S6, the three samples with the same mass of 500 mg are filled in the transparent bottles and the volume of the FeS@CNS is much larger than that of the FeS/C and FeS. Further characterizations showed that FeS nanoparticles with an average size of $\sim 20 \text{ nm}$ are uniformly anchored on the carbon nanosheets according to the TEM and HRTEM images (Fig. 3b-d). These carbon nanosheets not only function as a conductive substrate for electron/ion transfer, but also effectively buffer the large volume change of FeS during the lithium ions insertion/extraction processes. In addition, HRTEM image shows the well-defined lattice fringes of nanoparticles crystals, where the lattice spacings of 0.29 and 0.21 nm are consisted with the (110) and (114) crystalline planes of hexagonal FeS, respectively. These results are in accordance with the XRD analysis described above, further revealing a high degree of crystallinity of the FeS nanoparticles. To character the element distribution in the FeS@CNS, the elemental mappings of sulfur, iron and carbon at the selected area of STEM (Fig. 3e) are shown in Fig. 3f-h. The homogenous distribution of all these elements definitely proves that FeS nanoparticles are uniformly embedded in the carbon nanosheets.²⁶

Fig. 4a-c respectively displays the CV curves for the first three cycles of FeS particles FeS/C and FeS@CNS at a scan rate of 0.1 mV s^{-1} in the voltage window of 0.01-3 V. For FeS sample, three reduction peaks appear in the first cycle just as

the papers reported previously.^{33,37} The small peak at 1.7 V is corresponding to the formation of Li_2FeS_2 ($2\text{FeS} + 2\text{Li} + 2\text{e}^- = \text{Li}_2\text{FeS}_2 + \text{Fe}$) and the sharp peak at 1.1 V is resulted from the conversion reaction of $\text{FeS} + 2\text{Li} + 2\text{e}^- = \text{Li}_2\text{S} + \text{Fe}$.³³ The broad peak observed at about 0.7 V is usually from the side reactions on the interfaces of the electrode and the formation of the solid electrolyte interface (SEI) film.^{37,38} From the second cycle, the reduction peaks at 0.7 and 1.1 V shift to 0.8 and 1.3 V, respectively, and the oxidation peak at 1.9 V shifts to 2.0 V with a remarkable current density drop, which means some irreversible reactions occur in the first cathodic process.³⁷ As a result, the structure may not be stable during the discharge and charge process. Correspondingly, the oxidation peak for the first cycle at $\sim 1.9 \text{ V}$ is attributed to the oxidation of Fe to form $\text{Li}_{2-x}\text{FeS}_2$ ($\text{Fe} + \text{Li}_2\text{S} - x\text{Li} - x\text{e}^- \rightarrow \text{Li}_{2-x}\text{FeS}_2$) and the peak at $\sim 2.3 \text{ V}$ is related to the formation of Li_2FeS_2 .³⁸ These peak current densities decrease gradually with the peak potential shifting to positive direction upon cycling, implying the electrode polarization is aggravated, probably due to the sluggish reaction kinetics of pure FeS nanoparticles.^{37,38} For the FeS/C, the CV curves are similar to that of FeS, while the intensity of the oxidation and reduction peaks are much weaker due to the addition of the carbon. Compared with the CV curves of FeS particles and FeS/C, the peak current densities as well as the peak potentials of the FeS@CNS seldom change after the first cycle. And, only one single pair of redox peaks appears at ~ 1.3 (reduction) and 1.9 V (oxidation), the peak derived from the formation of SEI film disappear in the following cycles, suggesting the introduction of carbon nanosheets can effectively promote the formation of a stable SEI and consequently decrease the irreversible capacity for SEI consumption.^{28,33}

Fig. 4d-f show representative initial discharge/charge

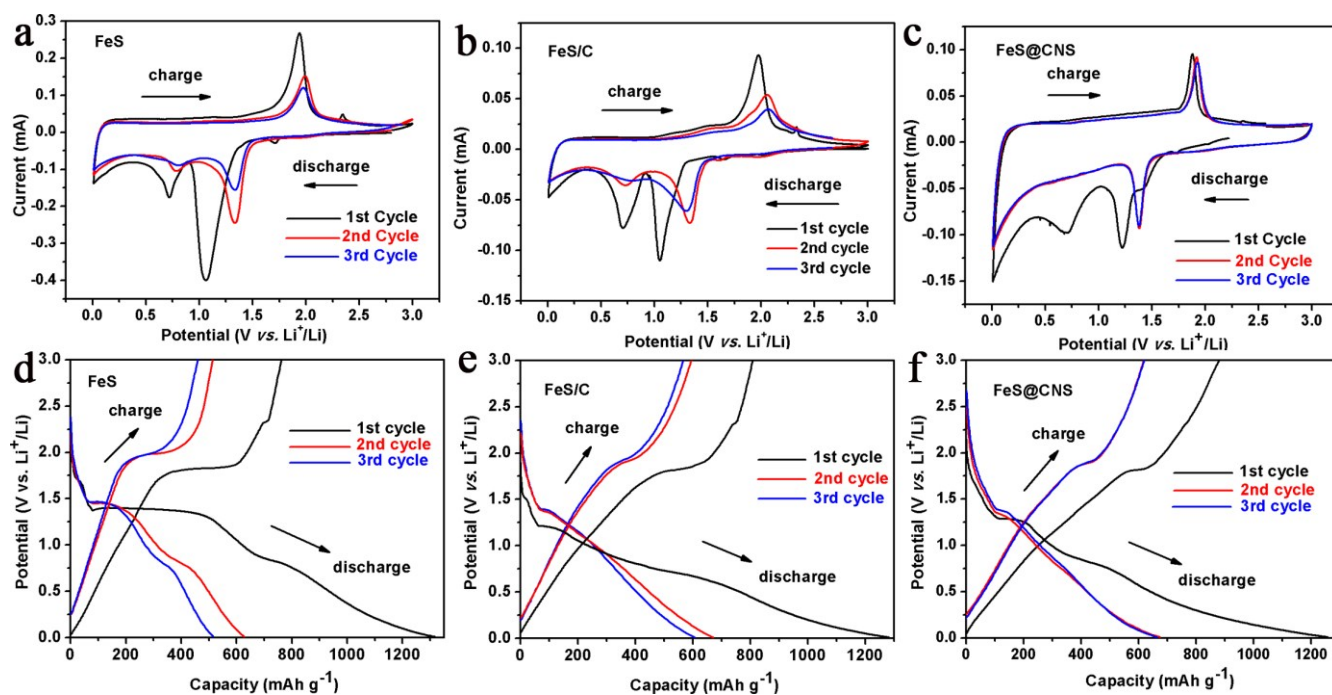


Fig. 4 (a-c) CV curves and (d-f) charge-discharge voltage profiles of FeS, FeS/C and FeS@CNS.

voltage profiles of the FeS nanoparticles, FeS/C and FeS@CNS, respectively. Upon the first discharge, three voltage plateaus at around 1.6, 1.3 and 0.8 V are found for the FeS nanoparticles. The distinct plateau at around 1.3 V is due to the lithiation process of forming Li_2S and Fe, while the plateaus at around 1.6 and 0.8 V are respectively resulted from the lithium ions insertion into the FeS host and the formation of SEI film.^{28,37} The plateau at 1.6 V is totally disappeared in the following discharging processes identifying with the CV results. Compared with the FeS, the potential plateaus of FeS/C and FeS@CNS are much shorter in accordance with the CV results. Only one short plateau at around 1.25 V for FeS@CNS can be clearly identified corresponding to the phase transition of FeS/Fe.^{37,38} Consequently, 1258 mA h g^{-1} are obtained for FeS@CNS during the first discharge process which is lower than that of FeS (1316 mA h g^{-1}) and FeS/C (1282 mA h g^{-1}). The charge voltage profiles are also consisted with the CV results and acquire 763, 807, 880 mA h g^{-1} for FeS, FeS/C and FeS@CNS, respectively, corresponding to a initial Coulombic efficiency of 58 %, 63% and 70 %. Although the capacities of FeS@CNS are lower than that of FeS and FeS/C, the initial Coulombic efficiency of it is significantly increased due to the introduction of conductive and stable carbon nanosheets.

Fig. 5a displays the cycling performance of FeS@CNS, FeS/C and FeS particles and corresponding coulombic efficiency of FeS@CNS at a current density of 1 A g^{-1} . For FeS@CNS, the capacity gradually decreased to 664 mA h g^{-1} during the initial

several cycles. Then, the capacity is continually increasing upon cycling and becomes stable at 703.8 mA h g^{-1} over 150 cycles with a coulombic efficiency above 99.0 %. This phenomenon was commonly illustrated by the activation process of electrode materials. During the initial cycles, due to the lithiation-induced mechanical degradation of electrode materials and the formation of a large amount of SEI upon the decomposition of liquid electrolyte, resulting in an irreversible capacity loss. However, as the stabilization of SEI layer and reactivation of material, capacity stabilization is often occurred.^{9,43-45} The capacities of FeS and FeS/C composites are only 177 and 180 mA h g^{-1} at the 150th cycle, respectively, much lower than that of FeS@CNS. In order to determine the percentage of capacity contributed by carbon nanosheets, the cycle performance of pure carbon nanosheets is also tested. About 303 mA h g^{-1} of capacity is obtained at the 150th cycle, and the capacity derived from the carbon nanosheets is estimated to be ~32 mA h g^{-1} in consideration of carbon weight percentage (~10.5 %) in FeS@CNS composite, suggesting nearly all the capacity is resulting from the reactions between Li^+ and FeS.³³ In addition, the rate capability of FeS@CNS is evaluated in **Fig. 5b and c**. The electrode delivers 652, 628, 598 and 532 mA h g^{-1} at the current density of 0.5, 1, 2 and 5 A g^{-1} , respectively. When the current density decreases to 0.5 A g^{-1} , a capacity of 672 mA h g^{-1} can be retained. These electrochemical performances are among the best results of FeS based materials in the reported literatures (**Table S1**).

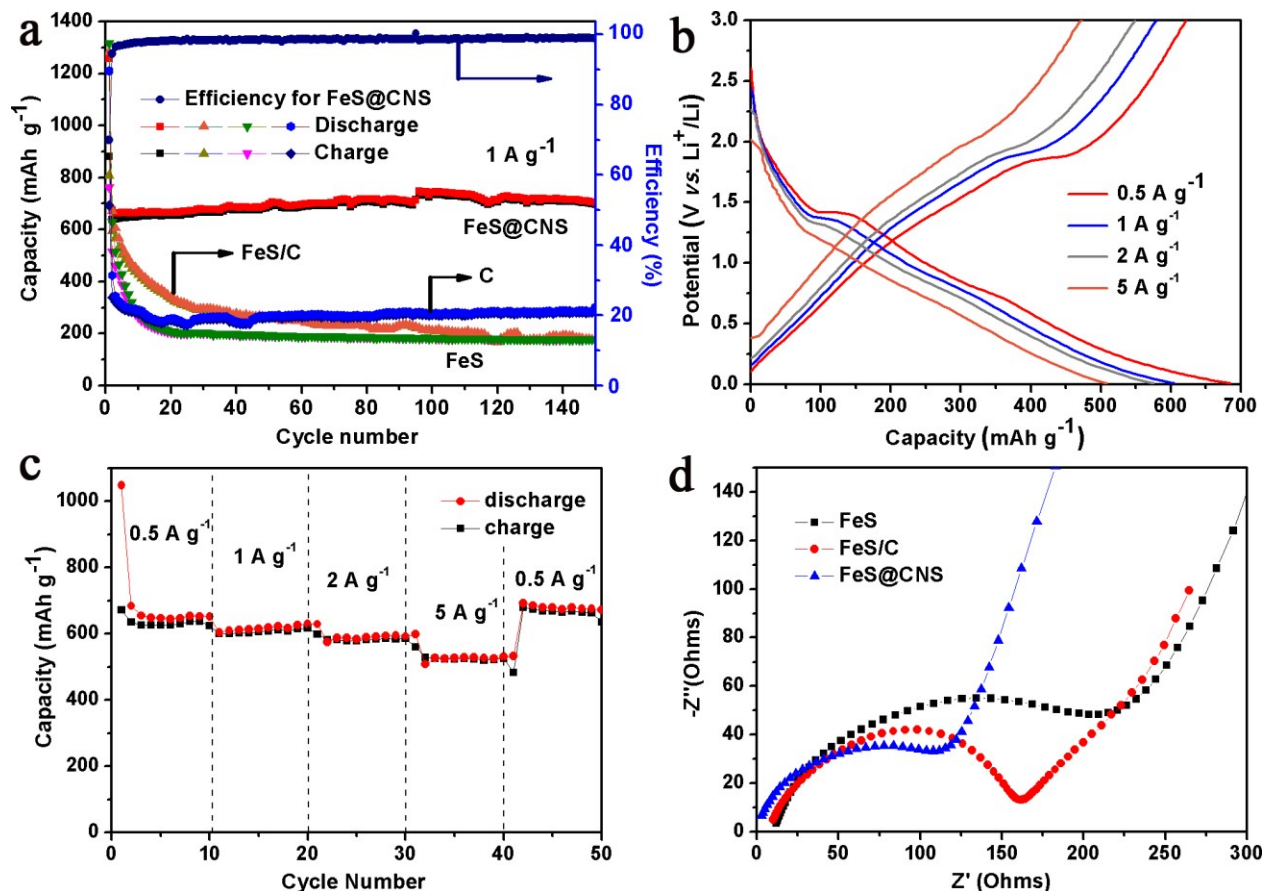


Fig. 5 (a) Cycle behaviors of FeS@CNS, FeS/C, FeS and C. (b) Charge and discharge profiles of FeS@CNS at different rates. (c) Rate capability of FeS@CNS. (d) Nyquist plots of FeS@CNS, FeS/C and FeS.

After the cycle measurement, the battery was further disassembled and the morphology of FeS@CNS was investigated. As evidenced by TEM images (Fig. S7), large carbon nanosheets with nanoparticles uniformly dispersing on it can be preserved, and the diameter of FeS nanoparticles after cycling are still similar to those before cycling as shown in Fig. 3, suggesting the robust structure stability of the FeS@CNS.³⁹ In addition, SEM images of the cross section of FeS@CNS, FeS, FeS/C anodes before and after cycling have also been tested. As exhibited in Fig. S8, all active materials closely attach to the current collectors before cycling. However, the FeS and FeS/C materials are more easily peeled off from the current collectors compared with FeS@CNS, which can be clearly demonstrated in their corresponding SEM images after cycling, suggesting the structure of FeS@CNS has better volume buffer effect during lithium ion insertion/extraction processes. In order to analyze the electrochemical kinetics of FeS@CNS, electrochemical impedance spectroscopy (EIS) measurements of different samples were performed and evaluated in Fig. 5d. All of these Nyquist plots are consisted by a medium-to-high frequency depressed semicircle and a low-frequency linear part. An equivalent circuit is exhibited as an inset in Table S2 where R_e is physical resistances, CPE_1 and R_f are the resistance and a constant phase element representing the SEI film, CPE_2 represents the double layer resistance, R_{ct} is charge transfer resistance which can be estimated from the diameter of the semicircle and Z_w is the Warburg resistance.^{26,37} Apparently, the R_{ct} value of FeS@CNS (36.4 Ω) is much smaller than that of FeS (84.5 Ω) and FeS/C (68.1 Ω) samples, implying the charge transfer process are successfully facilitated by the carbon nanosheets.

According to the above results, the improved electrochemical performances of FeS@CNS composite should be ascribed to the following reasons. First, due to the function of NaCl template, carbon nanosheets with large specific surface area can be easily obtained.^{26,39} These interconnected porous carbon nanosheets not only make the FeS nanoparticles avoid from agglomeration, but also provide a conductive matrix for electron/ion transfers during the electrode reactions. As a result, the battery performance of FeS@CNS is much better than FeS/C composite even their carbon weight percentages are similar. Second, the porous structure of FeS@CNS can be quickly infiltrated by the electrolyte during the initial cycles thus forming stable SEI films at the interfaces.²⁶ Third, the well-distributed FeS nanoparticles with small average diameter can provide sufficient electrode-electrolyte contact areas for high lithium ions flux across the interface and reduced lithium ions diffusion length, which significantly promote the electrochemical processes especially at high current densities.²⁸ Finally, the carbon nanosheets function as a stable and flexible host to anchor the FeS nanoparticles accommodating the volume change of FeS during the lithium ion insertion and extraction processes and preventing the active materials from detachment with current collector.^{26,39}

Conclusions

In summary, an interconnected porous FeS/carbon nanosheets (FeS@CNS) composite with FeS nanoparticles homogeneously embedded in carbon nanosheets was *in-situ* synthesized via a facile freeze-drying/carbonization method using NaCl as template. Owing to the hierarchical structure and the incorporation of carbon nanosheets with improved electron/ion conductivity, this FeS@CNS composite exhibits a significantly enhanced lithium-storage performance in terms of highly reversible specific capacity, good rate capability and much improved cycle stability. This FeS@CNS composite delivers a high reversible capacity of 703 mA h g⁻¹ after 150 cycles at 1 A g⁻¹ and enhanced high-rate capability (532 mA h g⁻¹ at 5 A g⁻¹), indicating its potential for LIB applications.

Acknowledgements

This project has been financially supported by National Natural Science Foundation of China (No. 51402343, 51302238), Shenzhen Municipality Project (No. JCYJ20140417113430618, JSGG20150602143328010), Guangdong Innovative and Entrepreneurial Research Team Program (No.2013C090,KYPT20141013150545116), and Scientific Equipment Project of Chinese Academy of Sciences (yz201440).

References

- 1 N. S. Choi, Z. H. Chen, S. A. Freunberger, X. L. Ji, Y. K. Sun, K. Amine, G. Yushin, L. F. Nazar, J. Cho, P. G. Bruce, *Angew. Chem. Int. Ed.*, 2012, **51**, 9994-10024
- 2 P. Poizot, S. Laruelle, S. Grugeon, L. Dupont and J. M. Tarascon, *Nature*, 2000, **407**, 496-499.
- 3 L. Ghadbeigi, J. K. Harada, B. R. Lettiere, T. D. Sparks, *Energy Environ. Sci.*, 2015, **8**, 1640-1650
- 4 W. Y. Li, Y. B. Tang, W. P. Kang, Z. Y. Zhang, X. Yang, Z. Yu, W. J. Zhang, C. S. Lee, *Small*, 2015, **11**, 1345-1351
- 5 W. Y. Li, Z. P. Li, W. P. Kang, Y. B. Tang, Z. Y. Zhang, X. Yang, H. T. Hong, C. S. Lee, *J. Mater. Chem. A*, 2014, **2**, 12289-12295
- 6 X. Y. Yu, H. Hu, Y. W. Wang, H. Y. Chen, X. W. Lou, *Angew. Chem. Int. Ed.*, 2015, **54**, 7395-7398
- 7 J. Wang, J. L. Liu, D. L. Chao, J. X. Yan, J. Y. Lin, Z. X. Shen, *Adv. Mater.*, 2014, **26**, 7162-7169
- 8 X. Wen, X. L. Wei, L. W. Yang, P. K. Shen, *J. Mater. Chem. A*, 2015, **3**, 2090-2096
- 9 H. T. Xue, D. Y. W. Yu, J. Qing, X. Yang, J. Xu, Z. P. Li, M. L. Sun, W. P. Kang, Y. B. Tang, C. S. Lee, *J. Mater. Chem. A*, 2015, **3**, 7945-7949
- 10 H. Liu, F. Zhang, W. Y. Li, X. L. Zhang, C. S. Lee, W. L. Wang, Y. B. Tang, *Electrochim. Acta*, 2015, **167**, 132-138
- 11 C. L. Tan, H. Zhang, *Chem. Soc. Rev.*, 2015, **44**, 2713-2731
- 12 H. Wang, H. B. Feng, J. H. Li, *Small*, 2014, **10**, 2165-2181
- 13 Y. C. Liu, Y. P. Zhao, L. F. Jiao, J. Chen, *J. Mater. Chem. A*, 2014, **2**, 13109-13115
- 14 Z. C. Wu, B. E. Li, Y. J. Xue, J. J. Li, Y. L. Zhang, F. Gao, *J. Mater. Chem. A*, 2015, **3**, 19445-19454
- 15 J. Wang, J. L. Liu, D. L. Chao, J. X. Yan, J. Y. Lin, Z. X. Shen, *Adv. Mater.*, **26**, 7162-7169
- 16 G. Wang, J. Peng, L. L. Zhang, J. Zhang, B. Dai, M. Y. Zhu, L. L. Xia, Feng Yu, *J. Mater. Chem. A*, 2015, **3**, 3659-3666
- 17 J. Liu, Y. R. Wen, P. A. van Aken, J. Maier, Y. Yu, *J. Mater. Chem. A*, 2015, **3**, 5259-5265

- 18 H. Jiang, D. Y. Ren, H. F. Wang, Y. J. Hu, S. J. Guo, H. Y. Yuan, P. J. Hu, L. Zhang, C. Z. Li, *Adv. Mater.*, **27**, 3687-3695
- 19 H. Hwang, H. Kim, J. Cho, *Nano Lett.*, 2011, **11**, 4826-4830
- 20 H. J. Yoo, A. P. Tiwari, J. T. Lee, D. Y. Kim, J. H. Park, H. Y. Lee, *Nanoscale*, 2015, **7**, 3404-3409
- 21 M. Acerce, D. Voiry, M. Chhowalla, *Nat. Nanotechnol.*, 2015, **10**, 313-318
- 22 S. Han, Y. R. Zhao, Y. P. Tang, F. Z. Tan, Y. S. Huang, X. L. Feng, D. Q. Wu, *Carbon*, 2015, **81**, 203-209
- 23 J. B. Ye, L. Ma, W. X. Chen, Y. J. Ma, F. H. Huang, C. Gao, J. Y. Lee, *J. Mater. Chem. A*, 2015, **3**, 6884-6893
- 24 J. Liu, Y. R. Wen, Y. Wang, P. A. van Aken, J. Maier, Y. Yu, *Adv. Mater.*, 2014, **26**, 6025-6030
- 25 J. Z. Wang, L. Lu, M. Lotya, J. N. Coleman, S. L. Chou, H. K. Liu, A. I. Minett, J. Chen, *Adv. Energy Mater.*, 2013, **3**, 798-805
- 26 J. W. Zhou, J. Qin, X. Zhang, C. S. Shi, E. Liu, J. J. Li, N. Q. Zhao, C. N. He, *ACS Nano*, 2015, **9**, 3837-3848
- 27 K. Chang, D. S. Geng, X. F. Li, J. L. Yang, Y. J. Tang, M. Cai, R. Y. Li, X. L. Sun, *Adv. Energy Mater.*, 2013, **3**, 839-844
- 28 C. B. Zhu, Y. R. Wen, P. A. van Aken, J. Maier, Y. Yu, *Adv. Funct. Mater.*, 2015, **25**, 2335-2343
- 29 D. T. Tran, S. S. Zhang, *J. Mater. Chem. A*, 2015, **3**, 12240-12246
- 30 C. C. Xing, D. Zhang, K. Cao, S. M. Zhao, X. Wang, H. Y. Qin, J. B. Liu, Y. Z. Jiang, L. Meng, *J. Mater. Chem. A*, 2015, **3**, 8742-8749
- 31 X. F. Wang, Q. Y. Xiang, B. Liu, L. J. Wang, T. Luo, D. Chen, G. Z. Shen, *Sci. Rep.*, 2013, **3**, 2007
- 32 C. C. Dong, X. D. Zheng, B. Huang, M. Lu, *Appl. Surf. Sci.*, 2013, **265**, 114-119
- 33 C. Xu, Y. Zeng, X. H. Rui, N. Xiao, J. X. Zhu, W. Y. Zhang, J. Chen, W. L. Liu, H. T. Tan, H. H. Hng, Q. Y. Yan, *ACS Nano*, 2012, **6**, 4713-4721
- 34 B. C. Kim, K. Takada, N. Ohta, Y. Seino, L. Q. Zhang, H. Wada, T. Sasaki, *Solid State Ionics*, 2005, **176**, 31-34
- 35 V. Yufit, K. Freedman, M. Nathan, L. Burstein, D. Golodnitsky, E. Peled, *Electrochim. Acta*, 2004, **50**, 417-420
- 36 E. B. Shangguan, F. Li, J. Li, Z. R. Chang, Q. M. Li, X. Z. Yuan, H. J. Wang, *J. Power Sources*, 2015, **291**, 29-39
- 37 L. Fei, Q. L. Lin, B. Yuan, G. Chen, P. Xie, Y. L. Li, Y. Xu, S. G. Deng, S. Smirnov, H. M. Luo, *ACS Appl. Mater. Interfaces*, 2013, **5**, 5330-5335
- 38 B. Wu, H. H. Song, J. S. Zhou, X. H. Chen, *Chem. Commun.*, 2011, **47**, 8653-8655
- 39 C. N. He, S. Wu, N. Q. Zhao, C. S. Shi, E. Z. Liu, J. J. Li, *ACS Nano*, 2013, **7**, 4459-4469
- 40 Y. S. Yun, D. H. Kim, S. J. Hong, M. H. Park, Y. W. Park, B. H. Kim, H. J. Kim, K. Kang, *Nanoscale*, 2015, **7**, 15051-15058
- 41 J. L. Liu, L. L. Zhang, H. B. Wu, J. Y. Lin, Z. X. Shen, X. W. Lou, *Energy Environ. Sci.*, 2014, **7**, 3709-3719
- 42 E. B. Hansson, M. S. Odziemkowski, R. W. Gillharn, *Corros. Sci.*, 2006, **48**, 3767-3783
- 43 J. Cabana, L. Monconduit, D. Larcher, M. R. Palacin, *Adv. Energy Mater.*, 2010, **22**, E170-E192
- 44 W. P. Kang, Y. T. Tang, W. Y. Li, X. Yang, H. T. Xue, Q. D. Yang, C. S. Lee, *Nanoscale*, 2015, **7**, 225-231
- 45 W. P. Kang, Y. T. Tang, W. Y. Li, Z. P. Li, X. Yang, J. Xu, C. S. Lee, *Nanoscale*, 2014, **6**, 6551-6556
- 46 H. Y. Jeong, Y. S. Han, S. W. Park, K. F. Hayes, *Geochim. Cosmochim. Acta*, 2010, **74**, 3182-3198
- 47 W. M. Skinner, H. W. Nesbitt, A. R. Pratt, *Geochim. Cosmochim. Acta*, 2004, **68**, 2259-2263

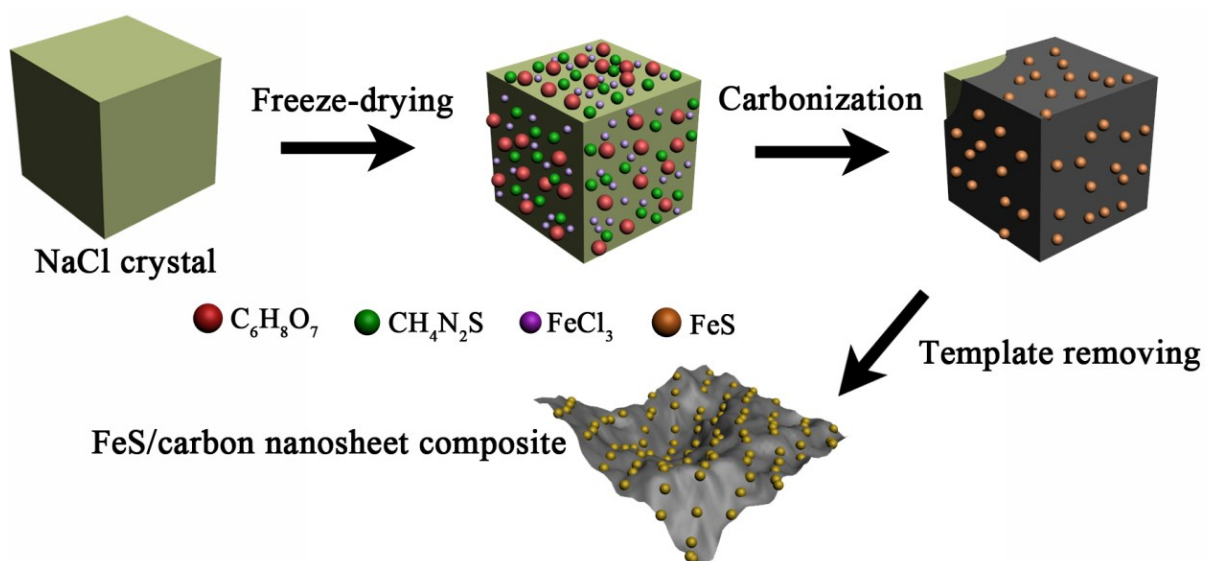


Table of Contents (ToC)

FeS nanoparticles embedded in porous carbon matrix with unique structure was successfully synthesized and shows impressive lithium ion battery performances.